Supporting information to

Barkhausen noise in the organic ferroelectric copolymer P(VDF:TrFE)

Andrey Alekseevich Butkevich, Marcel Hecker, Toni Seiler, Martijn Kemerink

Andrey Alekseevich Butkevich, Marcel Hecker, Toni Seiler, Martijn Kemerink

Institute for Molecular Systems Engineering and Advanced Materials, Im Neuenheimer Feld 225, Heidelberg, 69120, Germany.

Email: martijn.kemerink@uni-heidelberg.de

Contents

S1. Estimation of the number of switched dipoles in P(VDF:TrFE)

From sample geometry, the total number of switchable dipoles within a material N_t can be expressed as

$$N_t = \frac{P_s A_s D}{qd}.\#(S1.1)$$

Assuming a saturation polarization of $P_s = 110\, mC\, m^{-2}$,[1] a typical out-of-plane device with an active area of $A_s = 0.25\, mm \times 0.25\, mm$, a dipole moment of $D = 1.8\, Debye$,[2] the elementary charge q and the size of a macroscopic dipole d, **Equation S1.1** leads to a total of $N_t \approx 4.6 \cdot 10^{14}$ dipoles contributing to the switching of a typical out-of-plane P(VDF:TrFE) device. The minimal resolvable peak for P(VDF-TrFE) assuming a minimal detectable current of 4 nA for the optimal required sampling time of 1 µs (938 kHz sampling rate) results in $\sim 2.8 \cdot 10^8$ dipoles as the minimal number of simultaneously switching dipoles required for detection. Meanwhile, a critical volume of $4\, nm^3$ obtained from TA-NLS theory yields a magnitude of $\sim 10^3$ dipoles, not allowing a direct experimental observation in noise spectroscopy.

S2. Details on data acquisition and analysis

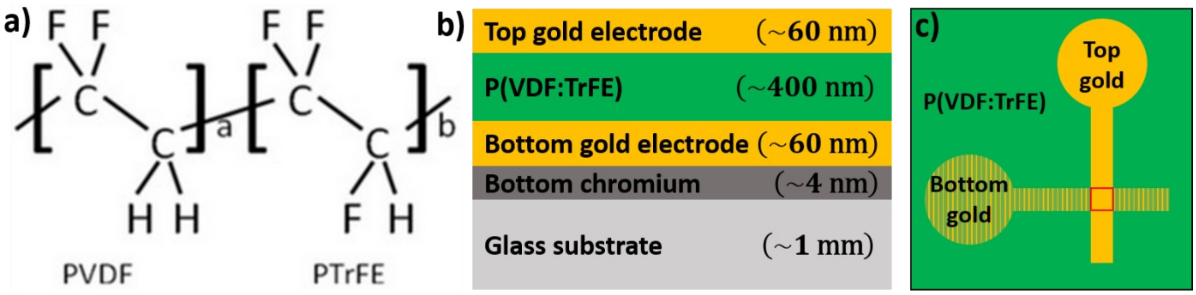

Figure S2.1: a) Chemical structure of the P(VDF:TrFE) random copolymer. The used ratio was 77% PVDF and 23% TrFE. **b)** Side and **c)** top views of an out-of-plane device used for ferroelectric characterization. The top view shows that the deposited electrodes have a well-defined cross-section (marked with a red square) where the electric field is applied. The bottom electrode is marked with stripes.

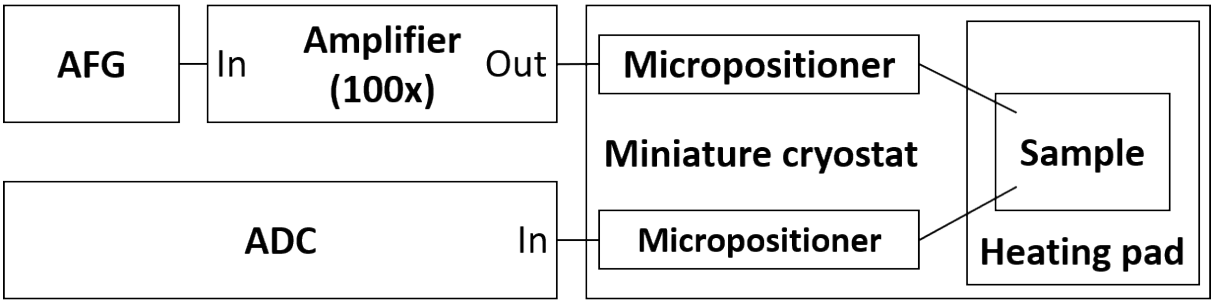

Figure S2.2: A schematic of the used measurement setup. The AFG is steered by a PC and applies a varying waveform signal which is amplified by an amplifier in order to reach the needed electric field strengths to the sample via contacting needle. The sample lies within a miniature cryostat which also allows to cool down and heat up the sample and simultaneously acts as a Faraday cage. The response voltage/current is measured by an analog-to-digital converter (ADC) which allows to trigger the signal and transfers it back to the PC for further analysis.

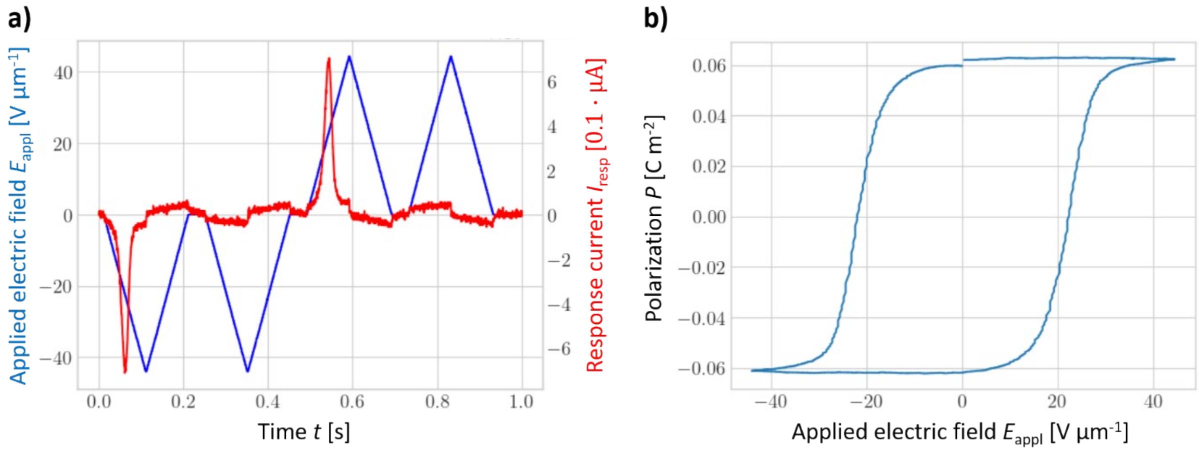

Figure S2.3: A typical switching current and the corresponding P-E-hysteresis loop of an out-of-plane P(VDF:TrFE) sample measured with a triangular double wave signal at 1 Hz and room temperature. **a)** The applied double wave voltage signal in both down and up directions (blue) and the corresponding sample response current (red). Here, the double wave is of triangular shape in order to obtain the hysteresis loop, as a truly square waveform does not allow to probe the response between the initial and final field values. In general, double wave signals allow to differentiate between the desired switching current and other contributions (like displacement and leakage) to the total current by subtracting the second (up or down) peak from the first.[3,4] Although this is necessary to obtain hysteresis loops as lossy dielectrics can exhibit hysteresis-like behavior[5], it is not needed for Barkhausen noise measurements as only the switching peak appearing at the first waveform peak is considered, so that a single waveform (as in PUND – positive up negative down) could be used instead. **b)** The corresponding polarization hysteresis loop obtained from the background corrected and integrated switching peaks.

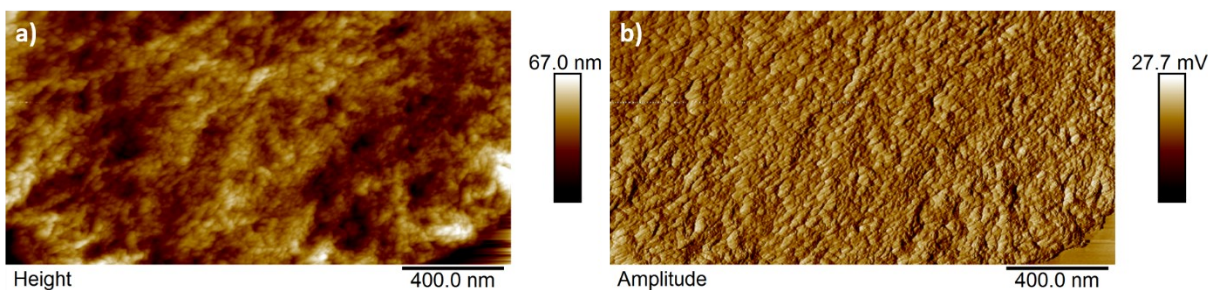

Figure S2.4: Typical AFM topology of a spin coated P(VDF:TrFE) sample (RMS: 18.3 nm) showing **a)** the height and **b)** the corresponding amplitude. While both the film thickness and the film roughness varied slightly between samples, the values were within the range of 300-400 nm and 15-25 nm, respectively. Both the topography and the roughness values are similar to other investigations for this compound.[6–9]

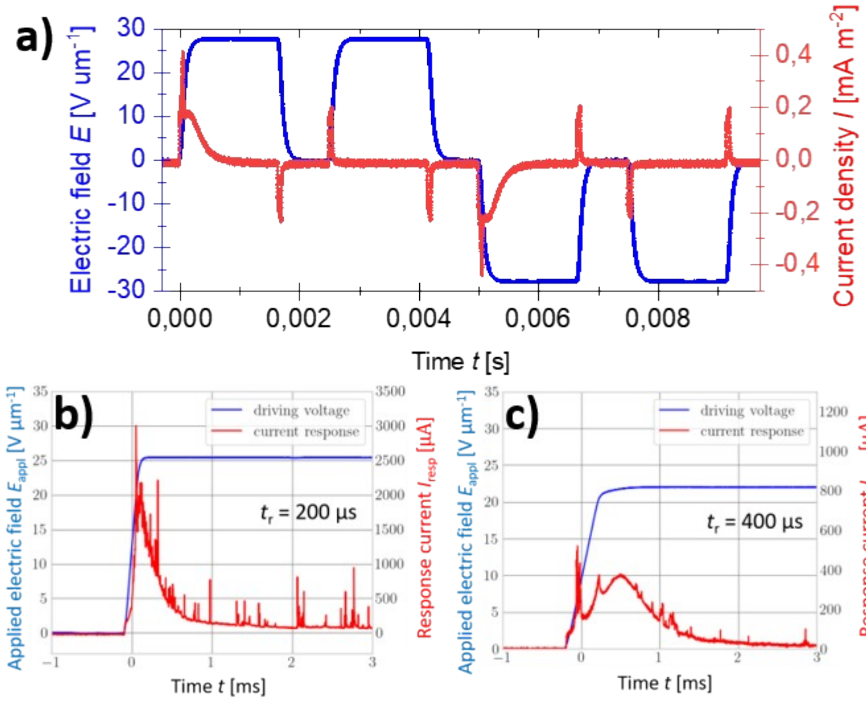

Figure S2.5: a) A measurement of current density of a P(VDF:TrFE) sample (red) in response to the applied electric field in form of a squared double wave (blue). Here, one measurement period is shown, the response current does not show well-developed Barkhausen noise. The applied wave form is a square double wave with variable rise times, meaning that the step-like increase is not instantaneous. The rounding of the applied electric field arises due to the used (input) noise-filtering circuit and has no effect on the measured response current from the sample. Same measurements with Barkhausen noise (sudden increases of the current response) showcasing the changes of the shape of the main switching peak depending on the ramp time of the square waveform for 200 and 400 µs rising times are shown in **(b)** and **(c)**, respectively. The current peaks after the voltage ramp arise as the sample is not fully switched during the ramp, since the applied electric field is near the coercive field.

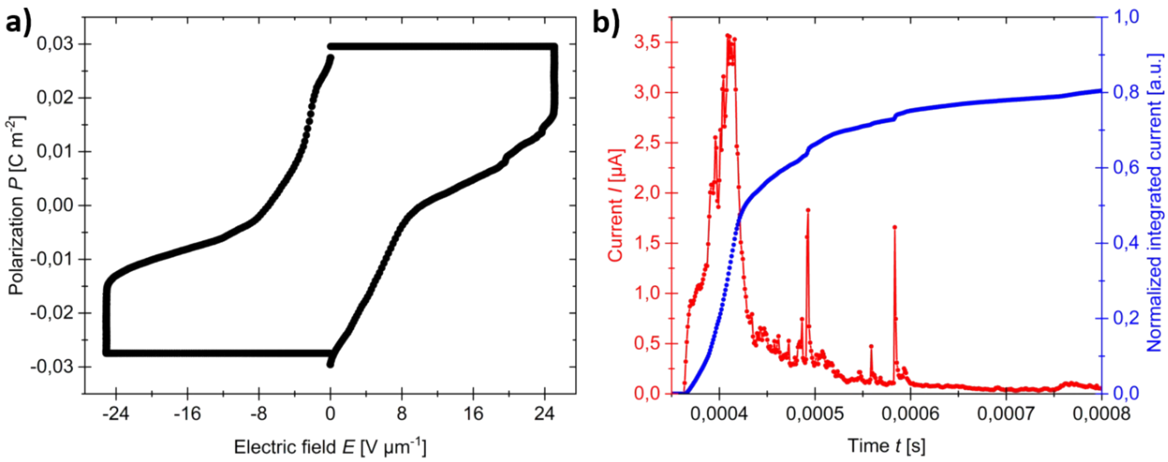

Figure S2.6: a) The P-E-hysteresis loop obtained by integrating the current measurement depicted in Figure 1a, where only the up-peak was shown. The odd shape can be explained by the used waveform and the fact that the measurement was carried out at a maximum electric field value close to the coercive field. The latter makes that the sample is not fully switched once the maximum field is reached, giving rise to the increasing polarization at the maximum applied electric field and to a polarization value of about half the saturated total remnant polarization value. Note also that the square waveform does not allow to determine the coercive field, as opposed to the triangular waveform, as shown in Figure S2.3. **b)** The normalized polarization zoomed-in on the part before the electric field ramp reaches its maximum value, similar to Figure 1c. Around 80% of the total polarization value is reached before the maximum electric field is applied. During the switching peak, no polarization jumps due to the signal spikes are apparent. While the integration of the two large signal spikes between 0.45 and 0.6 ms provides a visible increase in the polarization, the latter is within the values expected from larger domain wall movement. Importantly, switching spikes vanish for waiting times beyond those shown here.

Maximum likelihood fitting method:

For a power-law starting at a value x_{min} and having an exponent α, the probability $p(x)$ can be obtained via

$$p(x) = \frac{\alpha - 1}{x_{\mathrm{min}}}\left(\frac{x}{x_{\mathrm{min}}}\right)^{-\alpha}.\#(S2.1)$$

If there are *N* observations with $x_{\mathrm{i}} \geq x_{\mathrm{min}}$, the probability of the data fitting the model is proportional to

$$p(x|\alpha) = \prod_{i=1}^{N} \frac{\alpha - 1}{x_{\mathrm{min}}}\left(\frac{x}{x_{\mathrm{min}}}\right)^{-\alpha}.\#(S2.2)$$

The probability $p(x|\alpha)$ is the so-called likelihood. Maximizing the likelihood yields a better fit. Instead of the likelihood, the log-likelihood L – the logarithm of the likelihood – is commonly used. Considering the condition $\frac{\partial L}{\partial \alpha} = 0$, the maximum likelihood estimator $\hat{\alpha}$ is obtained [10]:

$$\hat{\alpha} = 1 + N\left[\sum_{i=1}^{N} \ln\left(\frac{x}{x_{\mathrm{min}}}\right)\right]^{-1}.\#(S2.3)$$

The corresponding calculations were implemented into a python package by Alstott et al. in 2014 and were used here for analysis and evaluation.[11]

Least squares (linear) method:

The aim of this probably most commonly used method for fitting models to data is to minimize the following expression:

$$\sum_{i=1}^{N}\left(y_{\mathrm{i}}-f\left(x_{\mathrm{i}}\right)\right)^2.\#(S2.4)$$

While the minimization can be done analytically for simple functions, the approach is typically non-trivial for non-linear functions. Many different algorithms exist to solve this problem. Within of this publication, the Levenberg-Marquardt algorithm was used.[12,13] A linear function $f(x)=mx+b$ is fitted to the measured data in double-logarithmic representation. Hence, the exponential of the fit function is plotted, which results in $f(x)=x^m e^b$, so that m is associated with the exponent α and e^b is just a constant.

S3. Experimental details

Amplifier characterization

Two amplifiers (TReK PZD350A and Falco System WMA-200) were tested, of which the latter was found to have the lowest noise level. To check that the provided amplification is the constant within the used frequency range, the specified amplification and bandwidth were verified by measuring the amplification at various frequencies using a sine wave input generated by an arbitrary function generator (AFG). Measurements both with and without a capacitor $(1\ \mu F)$ were done and the corresponding schematic as well as measurement results are shown in **Figure S3.1** and **Figure S3.2**, respectively.

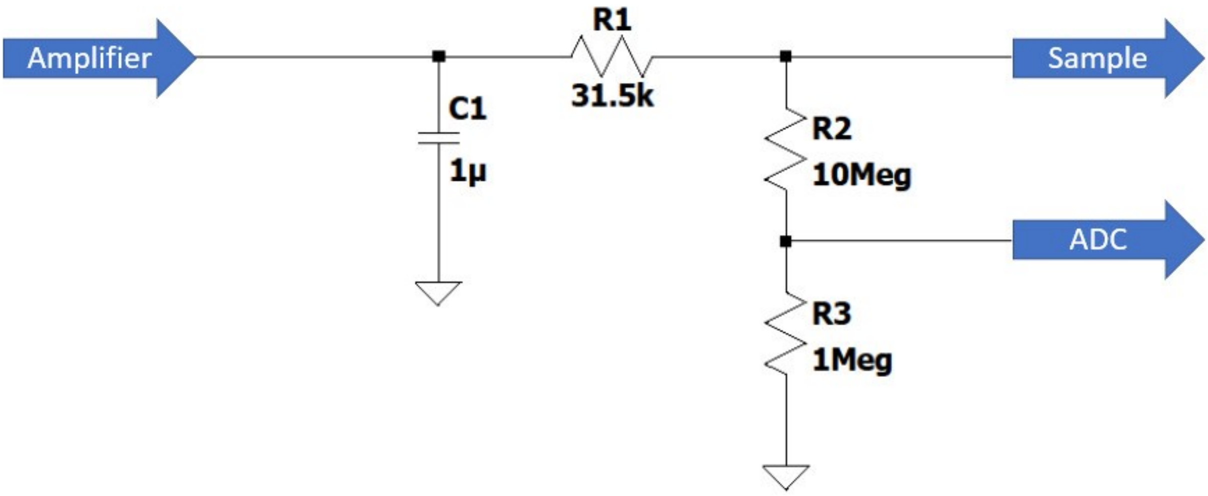

Figure S3.1: Circuit diagram of the measurement setup used for the amplifier characterization. Between the amplifier and the ADC, a RC-box is used in order to protect the instrument from excess voltage and current, which becomes especially relevant in case a sample short-circuits. It consists of three resistors of which one limits the current (R1) and the other two functioning as a voltage divider (R2 and R3). Additionally, a capacitor (C1) can be added to provide a base load to the amplifier, further reducing the noise level of the setup. The resistance values were chosen to obtain an advantageous division ratio considering the main voltage measurement input of $10\ M\Omega$ impedance and an auxiliary input of $1\ M\Omega$ impedance of the used ADCs.

The measured transfer function is fitted by the function

$$|H(f)| = \frac{G_o}{\sqrt{1 + \left(\frac{f}{f_c}\right)^2}} = \frac{|V_{in}|}{|V_{out}|} \#(S3.1)$$

with the maximum gain G_0 and critical frequency f_c. The function in **Equation S3.1** is the magnitude of the transfer function $H(f)$ for first-order low-pass filters.[14] **Figure S3.2** shows that the amplifier exceeds its specification for the frequency range (DC to $0.5\ MHz$) and is indeed sufficient for the conducted measurements. The slight drop in amplification at lower frequencies is caused by a built-in resistor which is in series with the measurement device, see **Figure S3.1**.

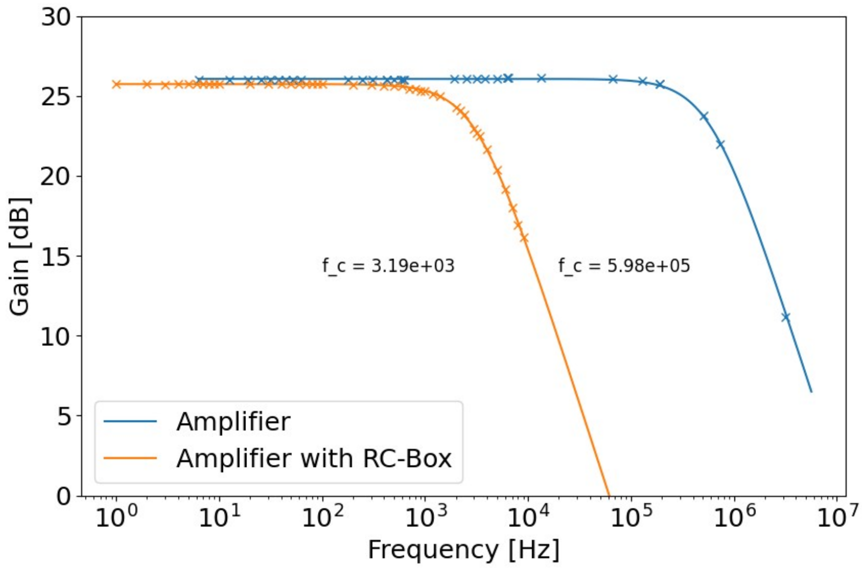

Figure S3.2: Measured amplification by TReK PZD350A high voltage amplifier of a sine signal generated by an AFG as a function of signal frequency f. The gain is plotted in decibels which equals to $20 \cdot log_{10}(|H(f)|)$. The measurements (crosses) were conducted with (orange) and without (blue) a capacitor $(1\ \mu F)$ and fitted (lines) with the function depicted in **Equation S3.1**.

Arbitrary function generator (AFG) characterization

Multiple AFGs (Keysight 33600A, Tektronix AFG3052C and Tektronix AFG1062) were compared to determine which provides the most suitable performance for the conducted measurements. The measurements were done by using a reference setup: The AFG output was connected to a TReK PZD350A 20× amplifier which led to the sample which was substituted with a dielectric reference capacitor (10 pF, the typical sample capacitance is 6 to 35 pF) and finally into the input of a Zurich Instruments MFLI lock-in amplifier that is used as a high-performance analog-to-digital converter (ADC). The current passing through the capacitor is measured as the $1\ M\Omega$ input impedance of the MFLI is used as a current-to-voltage converter. Since capacitors exhibit a current proportional to the displacement current, only current flow during constant voltage is considered. The MFIA's current range was set to $100\ \mu A$ with a sampling rate of $937.5\ kHz$. The obtained noise numbers and measured noise spectra are shown in **Table S3.1** and **Figure S3.3**, respectively. The Keysight 33600A AFG was deemed to be the best suited for measuring Barkhausen noise. The measurement of Keysight 33600A AFG was repeated for multiple setup variations to confirm its best performance which is shown in **Figure S3.4**.

AFG	**Noise number [nA]**
None (= noise floor of the MFIA/MFLI)	1.65 ± 0.03
Keysight 33600A	2.57 ± 0.13
Tektronix AFG3052C	4.92 ± 0.03
Tektronix AFG1061	12.41 ± 0.14

Table S6.1: Obtained noise numbers representing the noise levels of the tested AFGs. The measurements were done by using a reference setup in which the AFG output was connected to a 20× amplifier which led to the sample which was substituted by a dielectric reference capacitor with 10 pF (typical sample capacitance is 6 to 35 pF) and finally into the input of the Zürich Instruments lock-in (MFLI). Thus, the current passing through the capacitor is measured. Since capacitors exhibit a current proportional to the displacement current, only current flow during constant voltage is considered. The MFLI's current range was set to $100\ \mu A$ with a sampling rate of $937.5\ kHz$. The noise number is calculated using the standard deviation of the current.

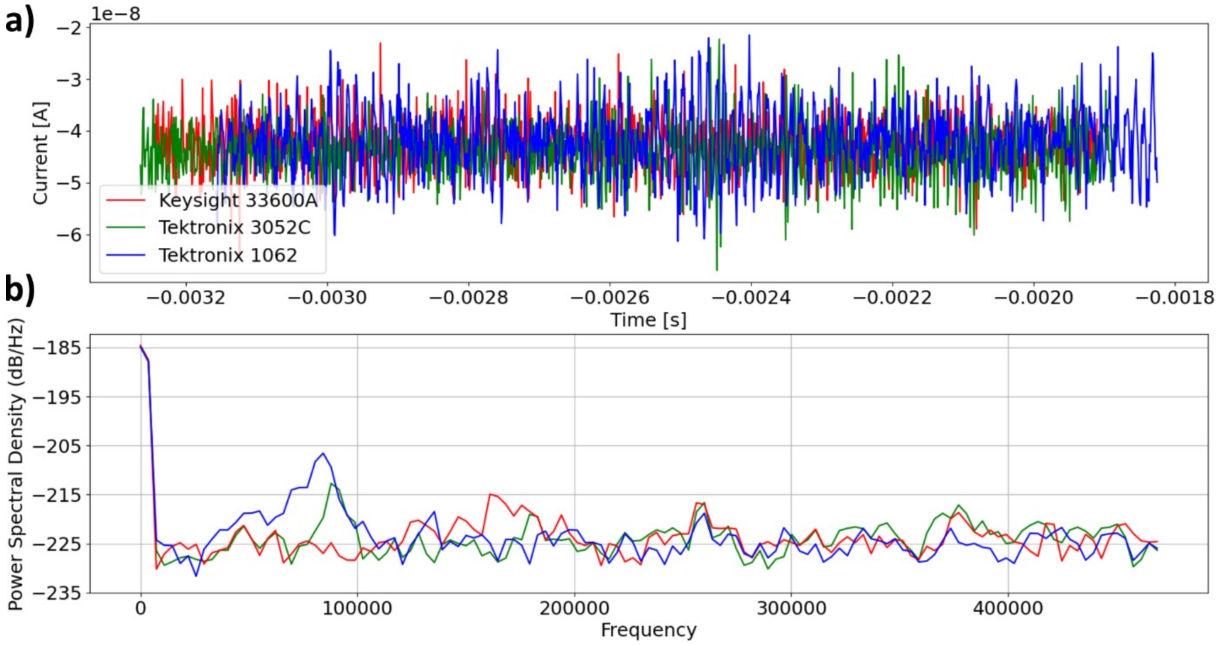

Figure S3.3: Noise measurements of the tested AFGs showing **a)** the measured current in the time domain and **b)** the corresponding power spectral density.

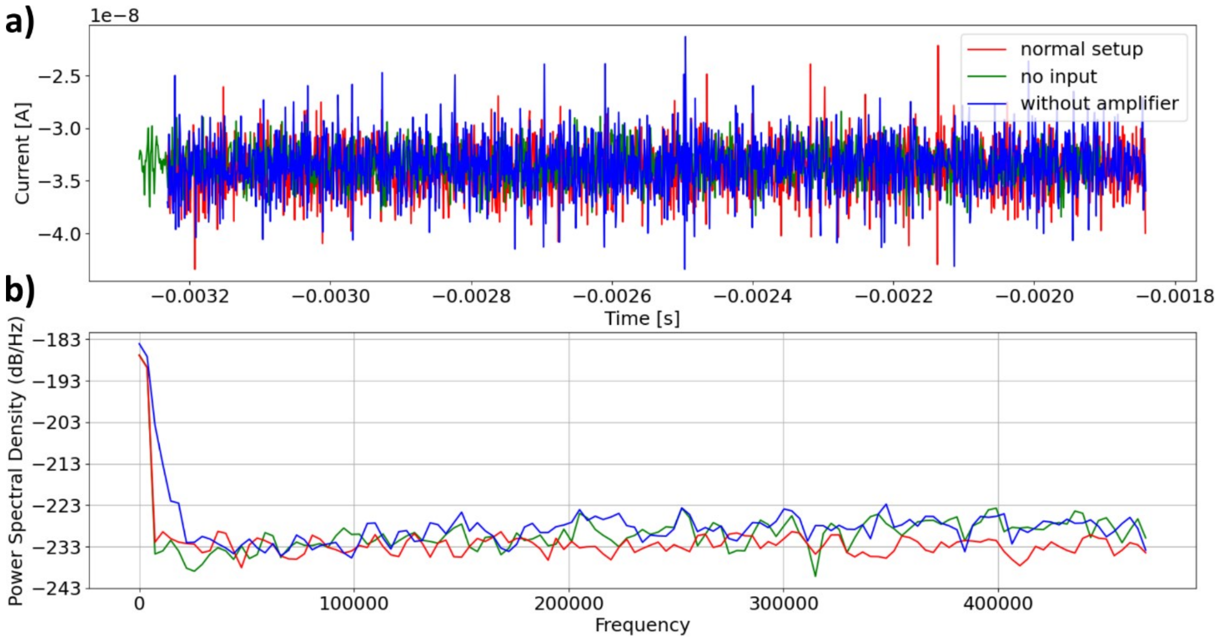

Figure S3.4: Noise measurements of the setup with Keysight 33600A Arbitrary Function Generator (AFG) showing **a)** the measured current in the time domain and **b)** the corresponding power spectral density. The noise of the entire setup without a device under test (red line), no input signal (green line, represents the noise floor) and setup without amplifier (blue line) are shown for comparison.

As mentioned in the main text, different rise times $\left((100{,}400\ and\ 800\ \mu s)\ {}^{+50}_{-0}\ \mu s\right)$ were investigated. However, it was discovered that the rise times slightly varied within the measurement series. E.g. the $100\ \mu s$ rise time measurement series encompasses rise times between $100\ and\ 150\ \mu s$. The same variability in rise times is present for both 400 and $800\ \mu s$. This variation in rise times is attributed to the feedback mechanism of the voltage amplifier reacting to the change in the capacitance of the ferroelectric samples with applied electric field.

Exclusion of charge trapping and release and breakdown phenomena

It is well known that thin film metal-insulator-metal devices can give rise to phenomena that bear a superficial similarity to Barkhausen noise, e.g. due to the formation of (unstable) conductive filaments[15,16] or charge trapping and release.[17] Some examples of such phenomena in similar devices as studied herein are shown and briefly discussed in (the supporting information of) Ref. [18]. In the present case, there are, however, several arguments that allow us to rule such scenarios as cause for the observed noise:

(i) Ref. [17] applies 100's of volts (up to 1 kV) to see the breakdown in the surface regions near the contacts of their devices, with sparking starting at approximately 200 V. The maximum voltage we apply is around 30 V.

(ii) Apart from applying much lower voltages than Ref. [17], we have much thinner films (approximately 0.4 µm vs 25 µm), about which Kliem et al. write (above their Fig. 5) "*Therefore at very thin dielectric films the peak discharges cannot be observed.*"

(iii) In Ref. [17], and consistent with the model therein, the sparks associated with charge trapping and release continue to appear all the way up to the maximum field (their Fig. 2a). In our case, the spikes density clearly correlates with ferroelectric switching, which in the case of our **Figure 1** leads to the peak density drastically dropping during the ramp, namely when the coercive field has been passed, and in the case of our **Figure S2.5b** and **c** leading to peaks occurring predominantly after the voltage ramp has ended, due to the fact that the ferroelectric switching lags behind the driving voltage. Neither effect can be explained in the 'artifact-discharge'-interpretation.

iv) Furthermore, we only apply electric fields below, at, and only slightly above the coercive field, meaning that our samples are not fully switched during the ramp, as shown in Figure S2.6.

This further explains the observed peaks after the ramp in Figure S2.5b and c, since the sample is still switching.

(v) We never observed the signals we interpret as Barkhausen noise in the second wave of the double wave response, which is inconsistent with filament formation or charge trapping and release.

vi) During the measurements, many samples were short-circuited, as is mentioned in Section 5 (Device preparation) in the main text. For clarification, we included all devices into the number, including the devices that short-circuited upon remeasuring after multiple measurements, etc. Although it may indicate that the devices are breaking over time, we could not establish a correlation between the amplitudes and number of appearing spikes and short-circuiting of the devices. We also never observed similar current peaks when trying to measure Barkhausen noise in BTA,[18] despite same device structure and similar film thicknesses between the electrodes.

vii) Finally, we compared our obtained current peaks with the ones arising from not fully and fully short-circuited samples. In both of the latter cases, the signals differed significantly, with larger amplitudes and different distributions of the current peaks (see iii). Integrating the current of such measurements yields 'polarization' values that are larger than expected from P(VDF:TrFE), and the jumps in polarization at the short positions are significant. We also tried to extract the power-law exponents from a short-circuited measurement, which yielded a hard-to-fit curve with exponents of significantly different values.

S4. Further experimental data

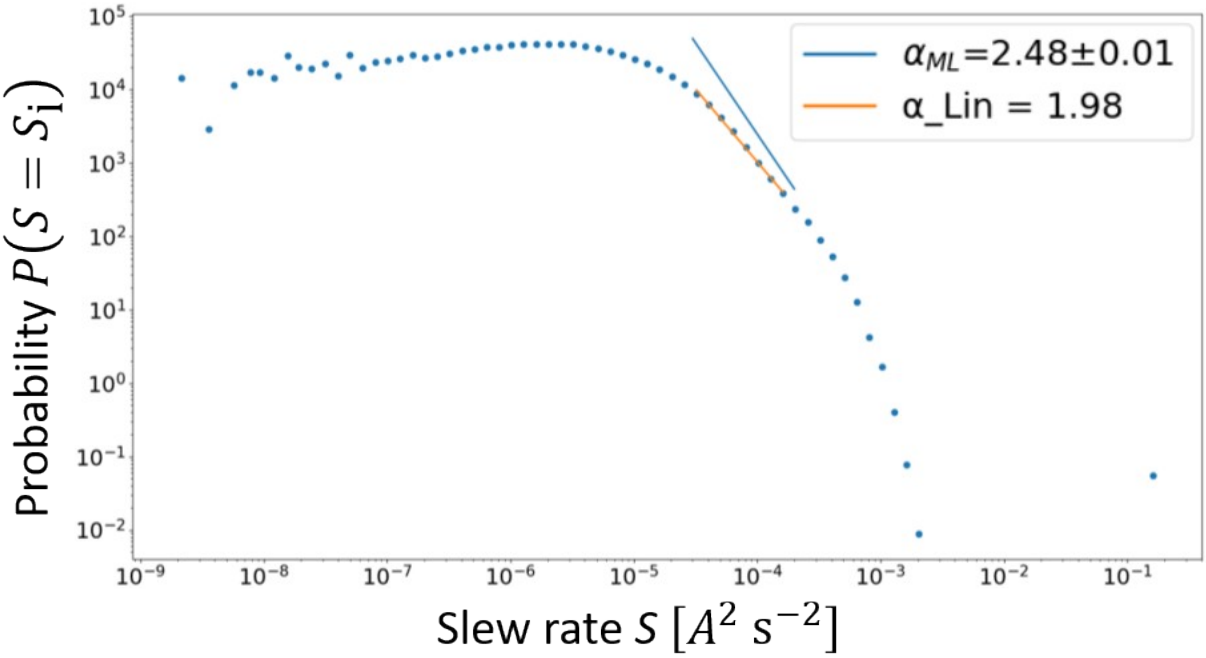

Figure S4.1: Measured histogram of the noise spectrum measured for a dielectric reference capacitor at $U = 9.9\ V$. The reference capacitor was put into the setup instead of a ferroelectric sample. No power-law behavior is observed over an extended range of slew rates. Instead, a plateau at lower slew rates is apparent, followed by a steep decline appearing as an exponential drop at a slew rate of $\sim 10^{-4} - 10^{-3}\ A^2 s^{-2}$. Furthermore, a peak at $\sim 0.4\ A^2 s^{-2}$ caused by the displacement current of the capacitor is visible. This reference measurement was used to rule out the possibility that only random noise was measured and was treated as a lower estimate for the noise floor.

Figure S4.2-4 show the measured histograms of P(VDF:TrFE) noise measurements for the three different rise times $\left((100{,}400\ and\ 800\ \mu s)\ {}^{+50}_{-0}\ \mu s\right)$ and different applied electric fields including the fits of the power-law exponents. Some histograms exhibit multiple power-laws and the corresponding fits were done where applicable. Some measurements deviate from the expected behavior which would be a plateau or slow decrease in the probability for lower slew rates, followed by a roll-off, containing the power-law behavior in its beginning part, followed by a steeper exponential drop at the largest event sizes.[19] For example, $19.8\ V$ for $100\ \mu s$ shows a second bump and $27.2\ V$ for $800\ \mu s$ initiates the power-law fit within the transitional region. In general, voltages corresponding to electric fields above the coercive field show a more pronounced transition region from the noise plateau (due to thermal fluctuations) at small event sizes to power-law like behavior. This is attributed to the power-law dominating the cut-off region, hence resulting in a direct transition from the plateau to the power-law.

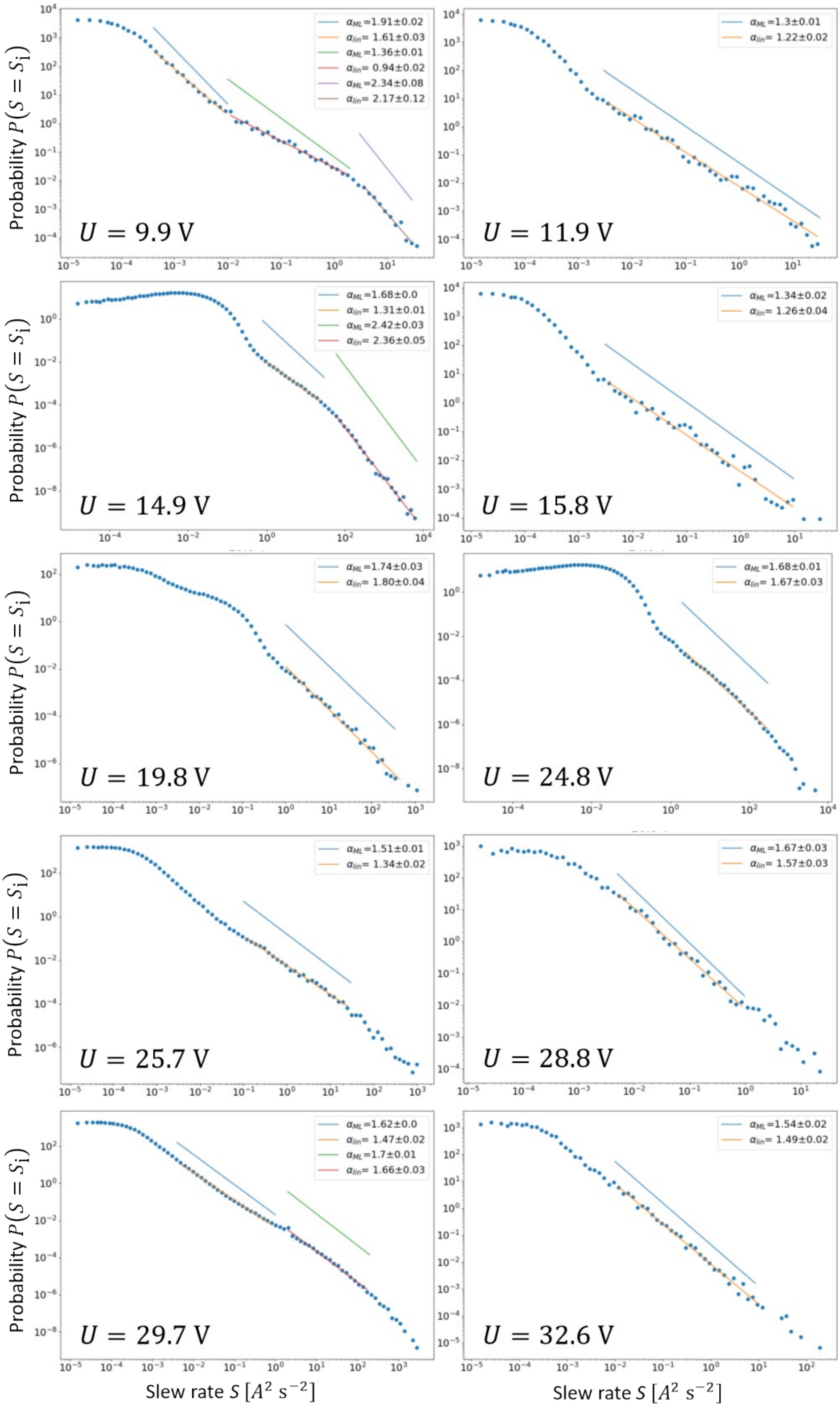
Probability $P(S = S_\mathrm{i})$
U = 9.9 V
α_{ML}=1.91±0.02
α_{lin}= 1.61±0.03
α_{ML}=1.36±0.01
α_{lin}= 0.94±0.02
α_{ML}=2.34±0.08
α_{lin}= 2.17±0.12
U = 11.9 V
α_{ML}=1.3±0.01
α_{lin}= 1.22±0.02
U = 14.9 V
α_{ML}=1.68±0.0
α_{lin}= 1.31±0.01
α_{ML}=2.42±0.03
α_{lin}= 2.36±0.05
U = 15.8 V
α_{ML}=1.34±0.02
α_{lin}= 1.26±0.04
U = 19.8 V
α_{ML}=1.74±0.03
α_{lin}= 1.80±0.04
U = 24.8 V
α_{ML}=1.68±0.01
α_{lin}= 1.67±0.03
U = 25.7 V
α_{ML}=1.51±0.01
α_{lin}= 1.34±0.02
U = 28.8 V
α_{ML}=1.67±0.03
α_{lin}= 1.57±0.03
U = 29.7 V
α_{ML}=1.62±0.0
α_{lin}= 1.47±0.02
α_{ML}=1.7±0.01
α_{lin}= 1.66±0.03
U = 32.6 V
α_{ML}=1.54±0.02
α_{lin}= 1.49±0.02
Slew rate S [A^2 s^{-2}]

Figure S4.2: Measured histograms of the $100\,\mu s$ P(VDF:TrFE) measurements at different applied electric fields with their extracted power-law exponents. Blue and orange lines are the fitted power-laws using the ML and LS (depicted as 'lin' here) fitting methods. The appearance of multiple sets of fits is due to the distribution seemingly showing multiple regions which may be identified as linear on the double-logarithmic scale. The final fit was chosen based on a combination of manual decision and minimizing the fit error.

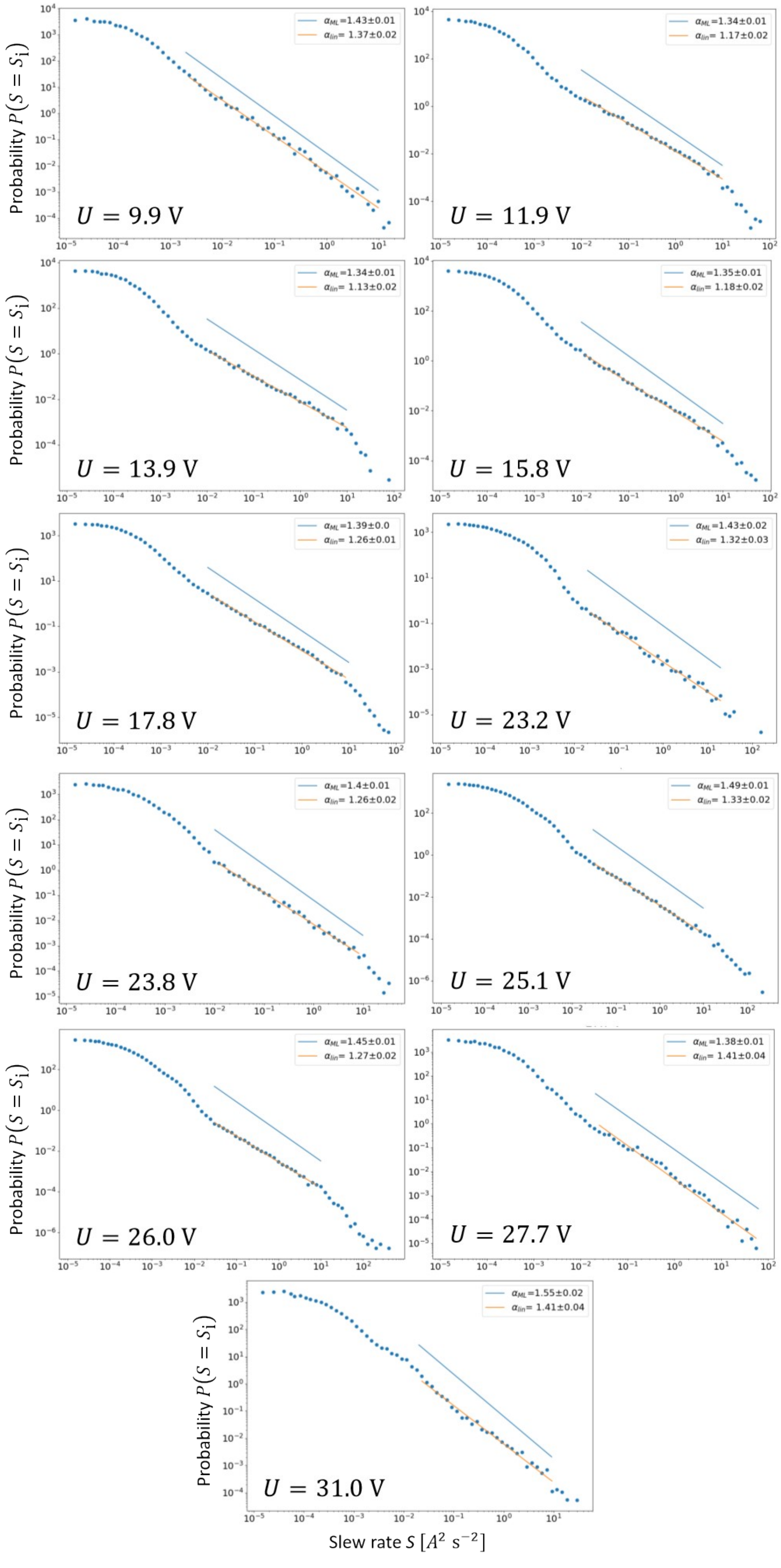

Probability $P(S = S_i)$
α_{ML}=1.43±0.01
α_{lin}= 1.37±0.02
$U = 9.9$ V
α_{ML}=1.34±0.01
α_{lin}= 1.17±0.02
$U = 11.9$ V
α_{ML}=1.34±0.01
α_{lin}= 1.13±0.02
$U = 13.9$ V
α_{ML}=1.35±0.01
α_{lin}= 1.18±0.02
$U = 15.8$ V
α_{ML}=1.39±0.0
α_{lin}= 1.26±0.01
$U = 17.8$ V
α_{ML}=1.43±0.02
α_{lin}= 1.32±0.03
$U = 23.2$ V
α_{ML}=1.4±0.01
α_{lin}= 1.26±0.02
$U = 23.8$ V
α_{ML}=1.49±0.01
α_{lin}= 1.33±0.02
$U = 25.1$ V
α_{ML}=1.45±0.01
α_{lin}= 1.27±0.02
$U = 26.0$ V
α_{ML}=1.38±0.01
α_{lin}= 1.41±0.04
$U = 27.7$ V
α_{ML}=1.55±0.02
α_{lin}= 1.41±0.04
$U = 31.0$ V
Slew rate S $[A^2\ s^{-2}]$

Figure S4.3: Measured histograms of the $400\ \mu s$ P(VDF:TrFE) measurements at different applied electric fields with their extracted power-law exponents. Blue and orange lines are the fitted power-laws using the ML and LS (depicted as 'lin' here) fitting methods.

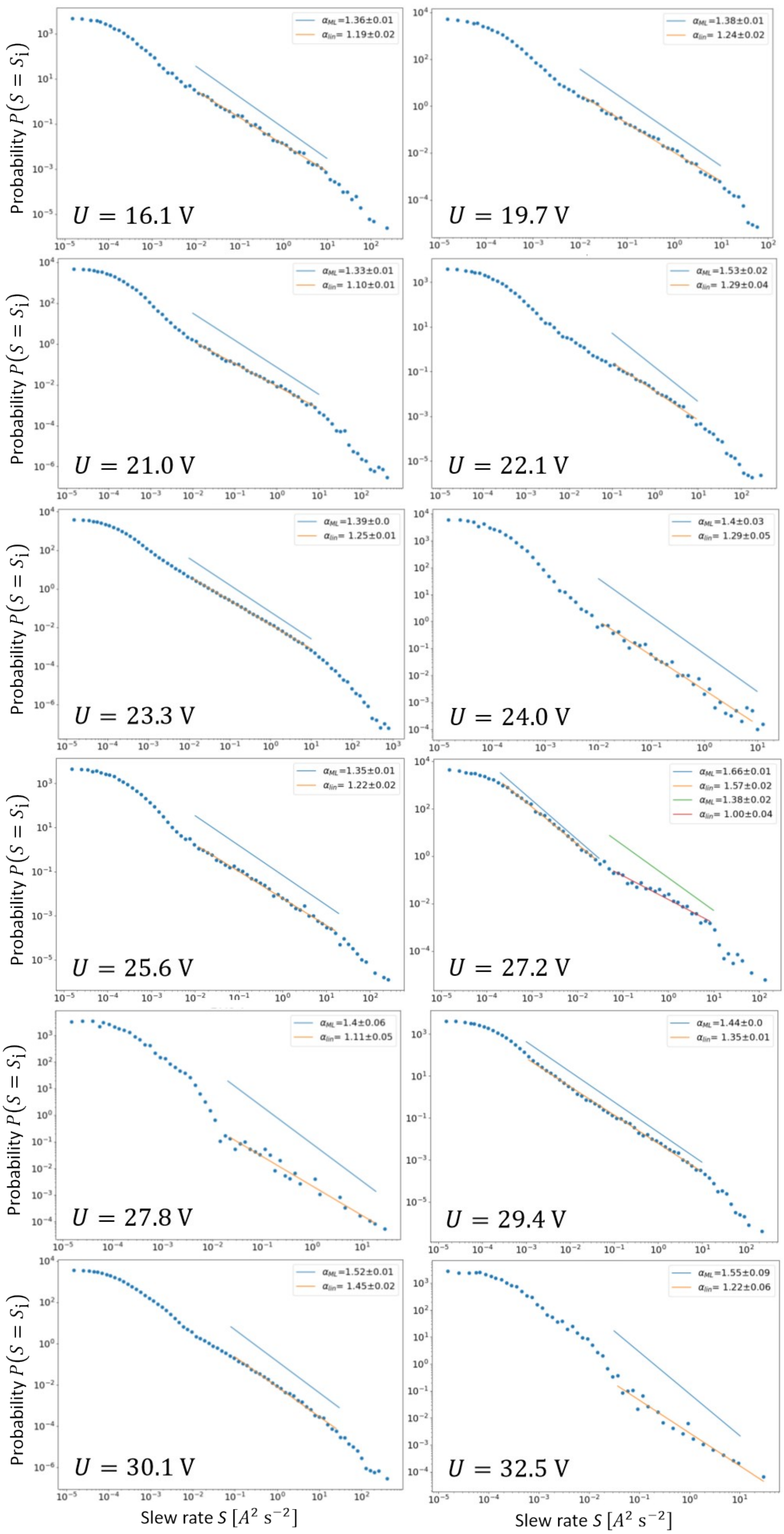
Probability $P(S = S_i)$
Slew rate S $[A^2\ s^{-2}]$
U = 16.1 V
α_{ML}=1.36±0.01
α_{lin}= 1.19±0.02
U = 19.7 V
α_{ML}=1.38±0.01
α_{lin}= 1.24±0.02
U = 21.0 V
α_{ML}=1.33±0.01
α_{lin}= 1.10±0.01
U = 22.1 V
α_{ML}=1.53±0.02
α_{lin}= 1.29±0.04
U = 23.3 V
α_{ML}=1.39±0.0
α_{lin}= 1.25±0.01
U = 24.0 V
α_{ML}=1.4±0.03
α_{lin}= 1.29±0.05
U = 25.6 V
α_{ML}=1.35±0.01
α_{lin}= 1.22±0.02
U = 27.2 V
α_{ML}=1.66±0.01
α_{lin}= 1.57±0.02
α_{ML}=1.38±0.02
α_{lin}= 1.00±0.04
U = 27.8 V
α_{ML}=1.4±0.06
α_{lin}= 1.11±0.05
U = 29.4 V
α_{ML}=1.44±0.0
α_{lin}= 1.35±0.01
U = 30.1 V
α_{ML}=1.52±0.01
α_{lin}= 1.45±0.02
U = 32.5 V
α_{ML}=1.55±0.09
α_{lin}= 1.22±0.06

Figure S4.4: Measured histograms of the $800\ \mu s$ P(VDF:TrFE) measurements at different applied electric fields with their extracted power-law exponents. Blue and orange lines are the fitted power-laws using the ML and LS (depicted as 'lin' here) fitting methods.

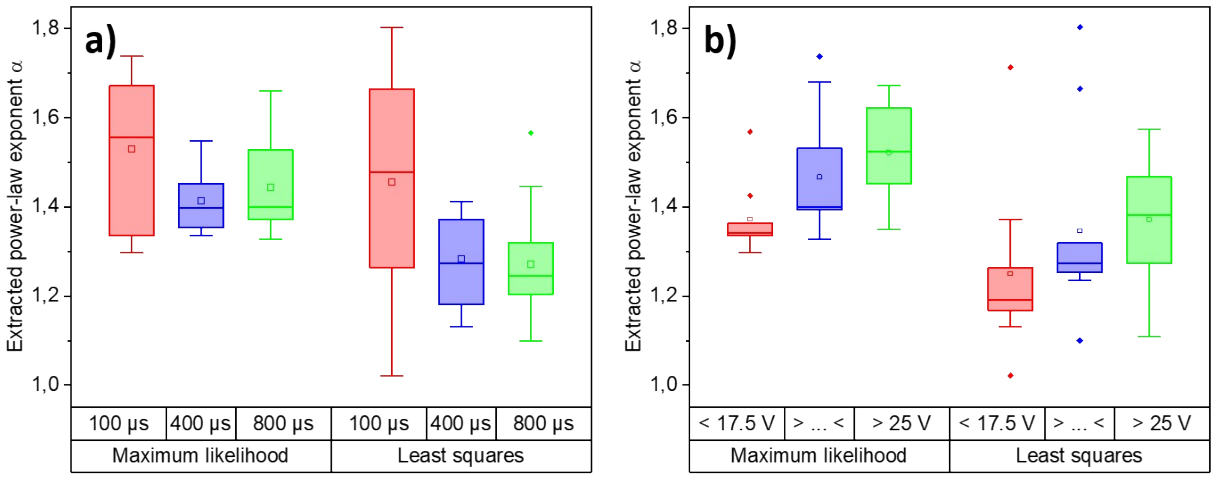

Figure S4.5: Box plot of the extracted critical power-law exponents α for **a)** the three different rise times and **b)** three different intervals of applied voltage for both fitting methods including all exponent values obtained from the histograms. The values obtained from ML fitting are slightly larger than from LS fitting for all three rise times, although here the difference between the values for $100\ \mu s$ is minimal. The trend of increasing exponents with applied voltage is clearly visible.

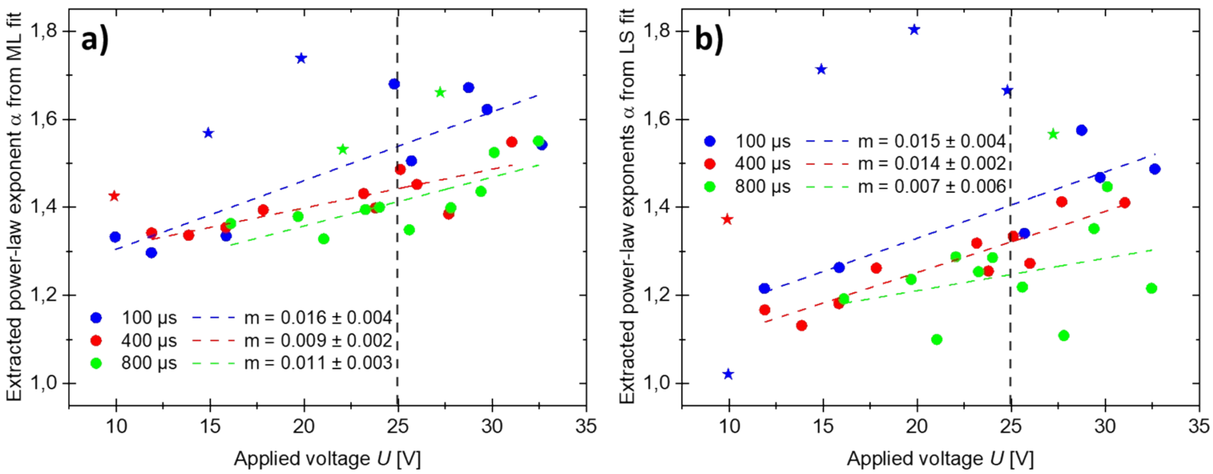

Figure S4.6: Power-law exponents α as a function of applied voltage U for three different rise times $(100\ \mu s\ (blue), 400\ \mu s\ (red)\ and\ 800\ \mu s\ (green))$ extracted from **a)** ML and **b)** LS fits of measured histograms. The extracted power-law exponents were fitted by a linear function to illustrate their trends, as indicated by the dashed lines. The corresponding slopes m are included in the plots. Some data points were deemed inconclusive based on the difficulty to obtain unique fits to the histograms and are marked as stars and were excluded from the linear fit. The coercive field of P(VDF:TrFE) is around $25\ V$ as marked by the vertical dashed black line.

Supplementary references

1 J. F. Legrand, Structure and ferroelectric properties of P(VDF-TrFE) copolymers, *Ferroelectrics*, 1989, **91**, 303–317.
2 T. Furukawa, Ferroelectric properties of vinylidene fluoride copolymers, *Phase Transitions*, 1989, **18**, 143–211.
3 A. V. Gorbunov, M. Garcia Iglesias, J. Guilleme, T. D. Cornelissen, W. S. C. Roelofs, T. Torres, D. González-Rodríguez, E. W. Meijer and M. Kemerink, Ferroelectric self-assembled molecular materials showing both rectifying and switchable conductivity, *Sci. Adv.*, 2017, **3**, e1701017.
4 M. Fukunaga and Y. Noda, New Technique for Measuring Ferroelectric and Antiferroelectric Hysteresis Loops, *J. Phys. Soc. Jpn.*, 2008, **77**, 064706.
5 J. F. Scott, Ferroelectrics go bananas, *J. Phys.: Condens. Matter*, 2007, **20**, 021001.
6 A. V. Solnyshkin, D. A. Kiselev, A. A. Bogomolov, A. L. Kholkin, W. Künstler and R. Gerhard, Atomic force microscopy study of ferroelectric films of P(VDF-TrFE) copolymer and composites based on it, *J. Surf. Investig.*, 2008, **2**, 692–695.
7 W. Li, Y. Zhu, D. Hua, P. Wang, X. Chen and J. Shen, Crystalline morphologies of P(VDF-TrFE) (70/30) copolymer films above melting point, *Applied Surface Science*, 2008, **254**, 7321–7325.
8 T. Feng, Xie ,Dan, Zang ,Yongyuan, Wu ,Xiao, Ren ,Tianling and W. and Pan, Temperature Control of P(VDF-TrFE) Copolymer Thin Films, *Integrated Ferroelectrics*, 2013, **141**, 187–194.
9 N. Jia, Q. He, J. Sun, G. Xia and R. Song, Crystallization behavior and electroactive properties of PVDF, P(VDF-TrFE) and their blend films, *Polymer Testing*, 2017, **57**, 302–306.
10 A. Clauset, C. R. Shalizi and M. E. J. Newman, Power-Law Distributions in Empirical Data, *SIAM Rev.*, 2009, **51**, 661–703.
11 J. Alstott, E. Bullmore and D. Plenz, powerlaw: A Python Package for Analysis of Heavy-Tailed Distributions, *PLOS ONE*, 2014, **9**, e85777.
12 K. Levenberg, A method for the solution of certain non-linear problems in least squares, *Quart. Appl. Math.*, 1944, **2**, 164–168.
13 D. W. Marquardt, An Algorithm for Least-Squares Estimation of Nonlinear Parameters, *Journal of the Society for Industrial and Applied Mathematics*, 1963, **11**, 431–441.
14 M. Poppe, *Prüfungstrainer Elektrotechnik*, Springer Berlin Heidelberg, Berlin, Heidelberg, 2018.
15 F. Verbakel, S. C. J. Meskers, R. A. J. Janssen, H. L. Gomes, M. Cölle, M. Büchel and D. M. de Leeuw, Reproducible resistive switching in nonvolatile organic memories, *Applied Physics Letters*, 2007, **91**, 192103.
16 M. Cölle, M. Büchel and D. M. de Leeuw, Switching and filamentary conduction in non-volatile organic memories, *Organic Electronics*, 2006, **7**, 305–312.
17 H. Kliem, A. Hessler and G. Arlt, in *1988. Annual Report., Conference on Electrical Insulation and Dielectric Phenomena*, IEEE, Ottawa, Ont., Canada, 1988, pp. 382–387.
18 A. A. Butkevich, F. T. Thome, T. Seiler, M. Hecker and M. Kemerink, Barkhausen noise in the columnar hexagonal organic ferroelectric BTA, *arXiv*, 2024, preprint, arXiv:arXiv:2412.12666, DOI: 10.48550/arXiv.2412.12666.
19 J. P. Sethna, K. A. Dahmen and O. Perkovic, Random-Field Ising Models of Hysteresis, *arXiv*, 2005, preprint, arXiv:arXiv:cond-mat/0406320, DOI: 10.48550/arXiv.cond-mat/0406320.